Influence of the manufacturing process on the interlaminar tensile strength of thick unidirectional continuous epoxy/carbon fibre composites

M. Grabow, V. Keryvin, A. Marchandise, J.-C. Grandidier, C. Baley, C. Le Guennec, O. Fagherazzi

Influence of the manufacturing process on the interlaminar tensile strength of thick unidirectional continuous epoxy/carbon fibre composites

M. Grabow[a], V. Keryvin[a,*], A. Marchandise[b], J.-C. Grandidier[c], C. Baley[a], C. Le Guennec[a], O. Fagherazzi[a]

[a] *Univ. Bretagne Sud, UMR CNRS 6027, IRDL, F-56321 Lorient, France*
[b] *Avel Robotics, F-56100 Lorient, France*
[c] *ISAE-ENSMA, UPR CNRS 3346, PPrime, F-86360 Chasseneuil-du-Poitou, France*

Abstract

Racing yachts that fly over the sea level use appendices called hydrofoils made out of carbon fibre reinforced plastics. This study discusses the influence of the manufacturing process on their interlaminar tensile strength (ILTS). Indeed, ILTS is a key design parameter, since tensile out-of-plane stresses in the hydrofoil elbow may cause the structure to fail by delamination. Hydrofoils are usually manufactured by traditional hand lay-up and more recently by automated fibre placement technology (AFP). Thick unidirectional L-beam specimens were manufactured from the same prepreg material, either by AFP or by hand lay-up (MAN). AFP specimens were 40 % stronger than MAN ones. The investigation of failure locations as compared to estimated ones made us highlight that AFP specimens reach their highest possible strength while MAN specimens fail prematurely, due to manufacturing-induced defects, such as localised porosities. The key features of AFP technology, with respect to the traditional MAN process, are eventually discussed.

Keywords: B. Delamination; E. Automated fibre placement (AFP); E. Prepreg processing; E. Lay-up (manual/automated); through-thickness tensile strength

*Corresponding author
Email address: vincent.keryvin@univ-ubs.fr (V. Keryvin)

1. Introduction

Hydrofoils have been revolutionising yacht racing these last ten years (America's Cup; Vendée Globe, sailing race round the world, solo, non-stop and without assistance) as they lift up boats out of the water, permitting to sail at higher speed over the sea. They are now usually made with continuous fibre reinforced plastics (CFRP; see Fig. 1). Those of IMOCA class (60 feet monohulls) weigh 250 kg, are 7 m long and 90 mm thick, while those of Ultim class (23- 32 m in length multihulls) weigh 450 kg, are 9 m long and 110 mm thick. In terms of dimensioning such appendices, the interlaminar tensile strength (ILTS), also referred to as through-thickness tensile strength, is one key design material parameter, along with the axial compression strength. The loadings-induced stress is either negative if the hydrofoil undergoes the dynamic lift (compressive state) or positive if the reverse case (tensile state) occurs. In the latter case, when the hydrofoil gets opened and the out-of-plane tensile stress reaches the ILTS, the elbow part fails by delamination. This situation is also at stake in aerospace or aeronautics (spars of centre wing boxes, flange-web transitions...).

The measurement of ILTS of layered composite materials has hence been a topic of high interest these last years [1, 2, 3] and several experimental methods exist [4, 5]. Jackson and Ifju [6] proposed a four-points bending (4PB) test configuration with advantages including a pure bending moment in the curved segment of a L shaped beam specimen or a self-aligning test configuration. The 4PB test configuration was later implemented in the standard [7]. It describes the determination of the ILTS of unidirectional L-beam specimens by 4PB using the analytical solutions of Lekhnitskii [8] and Kedward et al. [9].

Few works compared the mechanical response (other than ILTS) of CFRP with respect to the manufacturing process using prepreg semi-products. McManus and Mak [10] investigated the tensile failure and damage tolerance of (un)notched panel specimens made from graphite/epoxy (IM7/977-2, AS4/938) laminates. The specimens were manufactured by manual tape layup and by automated fibre (tow-preg) placement. Lan et al. [11] studied the influence of gaps and overlaps of CFRP specimens made from a Hexcel prepreg material on the microstructure, and on the tensile properties. The reference specimens were fabricated by hand lay-up and by AFP (automated fibre place-

ment) technology. Nguyen et al. [12] investigated the influence of gaps and overlap imperfections implemented in a controlled manner in flat non-unidirectional laminated specimens made from a Toray T800S/3900 prepreg. Panels were manufactured manually or by AFP.

Hydrofoils are usually manufactured by traditional hand lay-up, and more recently by AFP [13][1]. Advantages and drawbacks of both fabrication methods can be found in Kozaczuk [14]. Hand lay-up permits the production of complex and long shapes; expensive equipment is usually not required. The quality depends however on the skills of the operator. Ply cut operations prior to hand lay-up and intermediate debulking lead to long production times. Advantages of AFP are the producibility, the part to part repeatability, a low amount of material waste (no ply cut operations prior to lay-up), and sometimes a short production time. Furthermore, the robot head permits a constant contact pressure, permitting a uniform tacking of the plies, and a constant ply thickness. Limitations can be found in the application of the mould shapes.; for instance, the geometry of the robot head limits female mould radii. Ply edges at the end of a tape path represent a further drawback. Lan [15] emphasises that further advantages of AFP are the realisation of shapes with single or double curvature, or shapes with high variations in the thickness. Potter [16] reviewed sources of variability in the manufacturing of aircraft composite parts and how this leads to the generation of defects, such as voids, fibre misalignment, cure errors. *The comparison between two lay-up processes from prepreg semi-products, namely AFP and hand lay-up, on the out-of-plane tensile behaviour, is an open question that must be addressed.*

In some composite laminates, free edges may give rise to stress concentrations due to high interlaminar stresses and reduce ILTS. In other situations, ILTS might be only slightly reduced as reported by Charrier et al. [17] comparing unidirectional specimens and laminates. The laminates for masts or hydrofoils in racing yachts have usually 80-90 % of unidirectional plies contrary to aeronautics where quasi-isotropic stackings are widely used. Relatively few studies have focused on *thick unidirectional* specimens, and yet this knowledge is crucial for the nautical sector. Jackson and Martin [18] laid-up

[1] To our knowledge, the first hydrofoils made by AFP and used on multi-hulls have been manufactured in 2017 (ETF26 class, see Fig. 1) and 2019 (IMOCA class) by Avel Robotics.

unidirectional AS4/3501-06 carbon/epoxy prepreg plies and observed three delaminations but they had several load drops so that they could not capture the first delamination. No indication on the failure locus was given. Ranz et al. [19] laid-up unidirectional carbon fabrics and used the resin infusion process. They stated that rupture occurred at nearly one-third of thickness from the inner radius but no pictures of fractured specimens were given. Charrier et al. [17] tested unidirectional T700GC/M21 carbon/epoxy prepreg plies and observed that fracture occurred at between one-fourth and one-third of thickness from the inner radius but again no pictures of fractured specimens were given.

Thus, the topics the present paper would like to address are threefold. (i) Firstly, to our knowledge, no report has been made on the ILTS of AFP specimens, at least in pure bending. (Qian et al. [2] mimics the AFP-induced defects on hand lay-up specimens but the samples are not made by AFP.) (ii) Secondly, if several studies report the effect of a given manufacturing parameter on ILTS, no work has been dedicated to the comparison of different prepreg lay-up processes on ILTS. (iii) Lastly, the localisation of delamination is sparsely addressed on (thick) unidirectional specimens. In this study, the influence of the fabrication process of unidirectional CFRP L-beam thick specimens: hand lay-up of classical nautical quality (MAN) vs. AFP under industrial manufacturing conditions. Both types of specimens are made from the same prepreg material. Since both materials will be cured at the same time in an autoclave, it addresses more specifically the question of the influence of the lay-up process on the response of the L-beam specimen. The strength (ILTS) and the localisation of damage will be the indicators of the process quality, and a discussion about the impact of the manufacturing defects and their origin will put these results in perspective.

2. Materials and experimental methods

2.1. Materials

AFP and MAN L-beam specimens were made at Avel Robotics from 42 unidirectional plies, with a fibre weight of $300\,\mathrm{g/m^2}$, which were composed of carbon fibres with intermediate modulus IM2C from Hexcel and an epoxy matrix Se84LV from Gurit (glass transition $T_g \sim 115°C$, cf. datasheet `gurit.com`). The material for both L-beam types

came from a single prepreg roll with a 34.4 % resin weight content. For the AFP production, the material was slitted in eight spools of 6.35±0.125 mm in width tapes (slit-tapes). The theoretical ply thickness of the L-beams is 299 µm [20].

2.2. L-beam manufacturing

The fabrication of the MAN L-beam panel consisted in several steps. 42 plies were first cut from the material prepreg roll. After spyking the plies, as this is a common step in the nautical sector to ensure better resin flow during autoclave curing, the plies were laid-up by hand on an aluminium mould in 0°-direction. Uniform pressure with the thumbs at the corner of the mould and the gentle use of a spatula on the mould sides were exerted on each ply. Intermediate debulking under vacuum during 20 min at less than 1 bar was applied every 3 plies. The total lay-up processing time of the MAN L-beam panel was 9 h 20 min.

The manufacturing of the AFP L-beam panel was carried out by laying tapes on an aluminium mould with a C1-Coriolis Composites AFP robot in a one-shot sequence. Several tapes side by side formed thus one ply. The controlled lay-up contact pressure of the robot head of 5 bar, in connection to the local heating provided by the infra-red lamp (∼35-45 °C) which improves tacking, was assumed to be sufficient to ensure correct adhesion between the plies, and thus to avoid intermediate debulking. The total lay up processing time of the AFP L-beam panel was 1 h 05 min for the 42 plies. Figure 2 depicts the manufacturing process of the L-beam panel.

Thicknesses of both L-beam panels were then measured after the layup, and before curing, with a calliper. The thickness of the AFP panel was quite homogeneous along the span and width of the plate, with a mean thickness of 12.8 mm, resulting in a mean uncured ply thickness of 305 µm. The thickness of the MAN panel had a slightly higher mean thickness of 13 mm resulting in a mean uncured ply thickness of 309 µm. The thickness of the curved part of the MAN panel was generally slightly lower than that of the arms, and was more irregular through the width of the panel. Accurate measurements of the thicknesses across the span and width of the two panels could not be performed as easily on the uncured panels as on the cured ones (see below). Hence the uncured measurements and their analysis are here presented in a synoptical description, which seemed to be consistent with the measurement accuracy.

Both L-beam panels were cured simultaneously in an autoclave using a polycarbonate caul plate. Thermocouples were applied close to the mould and close to the caul plate side. The maximum pressure and temperature were 7 bar and 120 °C, respectively. Monitoring of the one-shot curing cycle had shown that neither the AFP nor the MAN L-beam panel underwent an exothermic reaction. A teflon layer that was applied on the aluminium moulds before laying up the first ply ensured correct demoulding without any significant panel deforming. Lastly, both panels were cut by mitre saw in approximately 25 mm wide L-beam specimens.

The thicknesses were then measured after curing at nine different points along the specimen thickness t using ImageJ2 software [21], as depicted in Figure 3, and reported in Table 1. The specimens' cross sections were drawn on a sheet, beforehand. The inner radii r_i and the angle between the horizontal and the specimen legs ϕ_i (undeformed state) were also measured. The specimen width w, determined at different points along the width, and length L were measured using a calliper. The outer radius r_o was calculated from the sum of inner radius $r_i = 6.4$ mm and specimen thickness t (see Fig. 4).

2.3. Experimental test procedure

Four-points bending (4PB) tests on seven AFP and seven MAN L-beam specimens were carried out according to the standard [7]. A schematic of the 4PB test setup is given in Figure 4. The diameter D of the loading bars was 20 mm, the upper and lower distances between the loading bar centres l_t and l_b were 82.7 mm and 91.5 mm, respectively. The loading bars were mounted with bearing bushes. The 4PB tests were carried out using a universal testing machine (Instron 8803, 50 kN load cell) and the applied force, P, was recorded. The vertical displacement speed was set to 0.5 mm/min. A linear variable differential transducer (type LVDT) was positioned beneath the specimen and the beam's deflection, u, was recorded. Digital image correlation (DIC, Gom Aramis 4M) was used for most of the L-beam specimens. The front side of the L-beam specimens was therefore sprinkled with black and white spray paint. As sudden specimen failure was expected, acoustic emission sensors (Mistras, R15 sensors) were positioned on some L-beams specimens for confirmation. After failure, specimens were cut

by water-cooled diamond sawing and cross-sections in the elbow were observed, after standard polishing procedures, by optical microscopy (Olympus BX51).

2.4. Data analyses

2.4.1. Analytical methods

ILTS was estimated according to two solutions proposed in the standard [7]. The solution from Lekhnitskii [8] was developed for curved mono-layered anisotropic cylinders subjected to an end moment, assuming plane strain conditions. The solution developed by Kedward [9] is based on the strength of materials.

For both solutions, first is computed the Curved Beam Strength (CBS), corresponding to the moment per unit width at failure, generated in the curved section of the L-beam specimen by the force $P_b = \frac{P}{2}$ acting on the lower loading bars, and the distance l_0 along the specimens' legs (see Fig. 4). The lever arm l_0 is given by:

$$l_0 = (D + t)\ \tan(\phi) + \frac{d_x}{\cos(\phi)}\ , \tag{1}$$

where d_x the horizontal distance between the vertical centreline of one upper and one lower loading bar.

The CBS is hence given by

$$\mathrm{CBS} = \frac{P_b l_0}{w} = \left(\frac{P}{2w\cos(\phi)}\right)\left(\frac{d_x}{\cos(\phi)} + (D + t)\tan(\phi)\right), \tag{2}$$

In order to obtain a more accurate estimation of the applied moment, the standard [7] recommends to use ϕ at failure, and not the initial value $\phi_i = 45°$ (experimentally measured), as its value changes during loading:

$$\phi = \sin^{-1}\left(\frac{-d_x(D + t) + d_y\sqrt{d_x^2 + d_y^2 - D^2 - 2Dt - t^2}}{d_x^2 + d_y^2}\right). \tag{3}$$

Eq. (3) is derived by trigonometric functions [7] with

$$d_y = d_x \tan(\phi_i) + \frac{D + t}{\cos(\phi_i)} - \Delta, \tag{4}$$

corresponding to the vertical distance between the horizontal centreline of one upper and one lower loading bar, and Δ representing the vertical stroke displacement during testing.

The Interlaminar tensile strength (ILTS), defined as the maximum radial stress at failure [7], is then determined according to Lekhnitskii [8] (noted $\mathrm{ILTS}^{\mathrm{L}}$) through

$$\mathrm{ILTS}^{\mathrm{L}} = -\frac{\mathrm{CBS}}{r_o^2 g}\left[1 - \frac{1-\rho^{\kappa+1}}{1-\rho^{2\kappa}}\left(\frac{r_{max}}{r_o}\right)^{\kappa-1} - \frac{1-\rho^{\kappa-1}}{1-\rho^{2\kappa}}\rho^{\kappa+1}\left(\frac{r_o}{r_{max}}\right)^{\kappa+1}\right] \tag{5}$$

with

$$g = \frac{1-\rho^2}{2} - \frac{\kappa}{\kappa+1}\frac{(1-\rho^{\kappa+1})^2}{1-\rho^{2\kappa}} + \frac{\kappa\rho^2}{\kappa-1}\frac{(1-\rho^{\kappa-1})^2}{1-\rho^{2\kappa}} \;\;,\;\; \kappa = \sqrt{\frac{E_\theta}{E_r}} \;\;,\;\; \rho = \frac{r_i}{r_o}\,, \tag{6}$$

and

$$r_{max} = \left[\frac{(1-\rho^{\kappa-1})(\kappa+1)(\rho r_o)^{\kappa+1}}{(1-\rho^{\kappa+1})(\kappa-1)r_o^{-(\kappa-1)}}\right]^{\frac{1}{2\kappa}} \;\;, \tag{7}$$

where κ represents an anisotropic parameter, r_i and r_o the inner and outer radii of the curved segment, r_{max} the position of the maximum radial stress, and E_r and E_θ the elastic moduli in the radial (out-of-plane) and circumferential (fibre) directions, respectively.

Kedward's approximate solution [9] (noted $\mathrm{ILTS}^{\mathrm{K}}$) is given by

$$\mathrm{ILTS}^{\mathrm{K}} = \frac{3\,\mathrm{CBS}}{2\,t\,\sqrt{r_i r_o}}\,, \tag{8}$$

where $\sqrt{r_i r_o}$ corresponds, according to Kedward et al. [9], to the radial location of the maximum radial stress.

These solutions were implemented into Python scripts and validated with respect to literature results [17].

2.4.2. Finite Element Analysis

Finite element simulations on each AFP and MAN L-beam specimen were performed in order to calculate the ILTS (referred to as $\mathrm{ILTS}^{\mathrm{EF}}$), as well as the stress fields along the specimen thickness and width in the curved segments of the L-beams. The commercial code Abaqus version 6.14 was used.

The 42 unidirectional plies were created with one linear volume element per ply thickness and ten elements through the width. The mechanical behaviour of the plies were taken as transversely isotropic linear elastic. The elastic properties, similar to those used in Keryvin et al. [22] for the same material, are given in Table 2. As depicted in Figure 5, the kinematics of the upper loading bars was linked to a reference point which could only move in z-direction, the movements in x- and y-direction being blocked. The lower bars were clamped. Regarding the composite part, the movement of the loading bars has been limited without constraining the L-beam specimen. In the plane of symmetry, a point has been blocked along x. Two points (one on each arm) were blocked along y to establish contact at the start of the simulation to remove rigid body degrees of freedom. The displacement in z-direction was determined by the contact, which was taken as strict (normal component of the reaction force) and frictionless (tangential component of the reaction force). The mesh was refined until differences of less than 1 % on the load-displacement curves were obtained. The loading bars were taken as rigid after finding that taking into account their deformability (steel loading bars) was of very little influence. A numerical model is built for each sample. After completion of the calculation, the $ILTS^{EF}$ (maximum radial stress) was determined at the experimentally recorded load at failure. The numerical model was validated by comparison to literature results [17], beforehand.

3. Results

3.1. Specimen metrology

Table 1 shows the mean values of the geometrical parameters for AFP and MAN L-beam specimens. The mean thickness values of both specimens types after autoclave curing differed only by 2.1 % from each other (12.89 mm for AFP and 13.16 mm for MAN specimens). It was found that for MAN L-beam specimens, the difference between the maximum and minimum thicknesses (averaged by batch) along the L-beam is 1.60 mm, approximately twice as high as that of the AFP L-beams (0.87 mm). MAN L-beam specimens were thinner in the curved part, and thicker in the specimens' arms. The AFP L-beam specimens have shown constant thicknesses along the span of each specimen, with very few thickness differences in the arm and the curved segment of the

specimens. Since the differences in geometry were hardly noticeable before curing and since the curing conditions were exactly the same for AFP and MAN, we can conclude that these subtle differences in geometry were exacerbated during curing.

3.2. Reproducibility and bending stiffness

Figure 6 shows the force-displacement curves of the 14 samples. An excellent reproducibility of the test realisation was found for both specimen types. Some non-linearity was observed at the beginning of the curves. This was due to the positioning of the LVDT which was not exactly in the symmetry plane at test beginning. The non-linear phase corresponded to a realignment of the measuring system with the specimen that stops after some time. Sample AFP-7 is an exacerbated example of this situation. Its stiffness, after 1 mm, is nonetheless the same as that of the other samples. Instantaneous failure, characterised by a strong force drop, was observed. This was confirmed by the acoustic sensors. Only data prior to load drop were kept. Table 3 shows the results of the AFP and MAN test campaigns in terms of bending stiffness and failure load. The bending stiffness of AFP specimens was 3742 $\pm$ 104 N/mm, that of MAN specimens was 3735 $\pm$ 104 N/mm, so no differences were noted.

3.3. Comparison analytical and numerical estimations of ILTS

Figure 7 shows the evolution of the out-of-plane tensile stress with respect to the radial position along the thickness or to the transverse position along the width of samples as calculated by FEA. The plane strain analytical estimation of Eq. (5) is also plotted. Figure 8 exhibits an example of the experimental and numerical force-displacement diagrams of L-beam specimen AFP-6. A very good correlation is found; the numerical model can be therefore used with confidence.

Table 4 shows the values of ILTS^{L} and ILTS^{K}, estimated through Eq. (5) and Eq. (8), respectively, as well as the FEM calculated ILTS^{FE}. It was found that Kedward et al. [9] solution is very close to the numerical calculation. In comparison, the solution of Lekhnitskii [8] differed from ~10-15 % from the numerical results. The somehow surprising better estimation of Kedward et al. [9] solution can be explained by replicating [9, Fig. 14] and adding the FE simulation results. Figure 9 depicts then the normalised maximum radial stress of the L-beams as a function of the degree of anisotropy κ and

of the specimen geometry. Using $\kappa = \sqrt{\frac{E_\theta}{E_r}}$ (Eq. (6)) and the material properties given in Table 2 (E_θ=E_1, E_r=E_2), the coefficient of anisotropy is $\kappa = 4.47$. As for the geometrical dimensions, is introduced the ratio $\frac{R_m}{t} = \frac{r_i + r_o}{2t} \sim 1$ (for this study), with R_m representing the mean radius of the curved L-beam segment. Figure 9 thus shows that the ILTS obtained by Kedward et al. [9] solution is almost equal to that of FEM, and that the solution of Lekhnitskii [8] results in clearly smaller ILTS estimations. Whether the solution of Kedward et al. [9] or Lekhnitskii [8] is closer to the numerical calculation depends hence on the elastic properties of the material. This is not mentioned in the standard [7] that states that less than 2% difference is found between the two analytical estimations, for usual CFRP. This is true for low thicknesses but not for high values as in this study.

The AFP and MAN L-beam specimens are now compared in terms of their loads at failure ILTS. As seen in Fig. 6, AFP L-beam specimens failed at higher loads (6661 ± 427 N) than MAN ones (3983 ± 740 N), see Table 3. Table 4 reports the ILTS^{K} mean values of both specimens types. The mean ILTS of the MAN specimens was approximately 40.2 % lower than that of AFP specimens. Moreover, the coefficient of variation (ILTS^{K}) was three times higher for MAN than for AFP specimens (17 % vs 6 %).

3.4. Location of the first crack

Figure 10 shows an example of how instrumentation permits to correlate the time and location of the onset of the first failure crack on the edges of a specimen. The sudden drop in force is associated to the occurence of a strain discontinuity (DIC) and a violent acoustic event in terms of energy, localisation and intensity (AE).

Theoretical first failure crack locations were determined analytically using Eq. (7) (r_{max}) from Lekhnitskii [8]. The relative quantity, $\gamma = \frac{r_{\text{max}} - r_i}{t}$, was estimated to be 0.34 and 0.32 for AFP and MAN L-beam specimens, respectively. The small geometrical differences (see Table 1), had no influence on this number. The variability on the analytical prediction of the location of the first failure crack was ± 0.02, calculated from the ply ($\sim$ 0.3 mm) and the specimen thicknesses, so that the expected failure location should lie between plies 13 and 16. Theoretical first failure crack locations were also determined with the theoretical failure location ($\sqrt{r_i r_0}$) from Kedward

et al. [9]. Values of 0.37 ± 0.02 and 0.36 ± 0.02, respectively for AFP and MAN, were found for the relative quantity γ. The first failure crack locations r_{FE} numerically calculated were determined at the locus of the highest out-of-plane stress (see Fig. 7), at $\gamma \sim 0.32$, hence equal to the value found analytically.

The number of cracks observed on the edges is around 3 for AFP samples and 1 for MAN samples (see Table 3). The experimental first failure crack location $r_{failure}$ of all AFP and MAN specimens are recapitulated in Table 4, in terms of the relative quantity γ. None of the seven MAN specimens had a γ close to the theoretical values (see Table 4), while five out of seven AFP specimens were in this case.

Figures 11 and 12 are post mortem observations by optical microscopy of the cross-sections of L-beams in the elbow where the cracks are located, for samples MAN-4 and AFP-6, respectively, along with associated side views of the edges. For some MAN samples (as in Fig. 11), some localised porosity can be observed between some plies. These observations are made for samples where the location of failure is different from the estimated one and for which (for instance MAN-4 Fig. 11) the ILTS values are the lowest. For all MAN samples, the crack is straight through the width, so that its location on the face is the same as inside. Actually, the crack always runs on two plies. Most of its path is intralaminar; it is interlaminar only when areas of porosity are observed. The position of the crack in the center coincide with that on the edges. In sharp contrast, with AFP (see Fig. 12), the localised areas of porosity, when observed, are much smaller than for MAN samples. The crack is translaminar, running through several plies (up to 6). Actually, the crack probably originating from the inside of the sample (the maximum stress is in the middle plane, see Fig. 7) propagates through the thickness and branches many times, so that many cracks reach the free surfaces. The difference between the location of the initiation crack and the positions of the observed cracks on the edges may differ by up to 3 plies in the different samples (see Fig. 12). This post-mortem method of defects inspection is not comprehensive. The use of micro-tomography as in Makeev et al. [4], Nikishkov et al. [5] is not made. Nevertheless, we highlight here the difference in the type of defects and their location and propagation generated by each lay-up condition rather than trying to describe completely the defect geometry.

4. Discussion

4.1. Influence of manufacturing process on geometry and defects

With regard to the production process of the two specimen types, the following similarities and differences can be noted. MAN and AFP L-beam specimens were made from the same prepreg material under industrial manufacturing conditions. They were laid-up on the same aluminium mould and underwent the same curing cycle. Their dimensions highlight that if the mean behaviour of both processes is identical, their specificities induce geometrical differences in terms of regularity. The robot compacted every ply with a lay-up contact pressure of $\sim 5\,\mathrm{bar}$, and the action of its compaction was always perfectly in line with the normal of the mould surface, resulting in constant ply thicknesses. Such a constant pressure could not be obtained by laying-up plies with thumbs and the spatula as this was the case for the hand lay-up fabrication, even if professionally-made in classical nautical yard conditions. MAN L-beam specimens were only compacted under vacuum every 3 plies. The vacuum compaction acted normally to the surface of the prepreg and not normally to the mould. The ply thickness before each intermediate debulking depended on the manual application and was not uniform all over the part. The developed length of the third ply of each sequence was always longer than the developed length of the first and second plies. The first aspect may be responsible for the apparition of surface irregularities on the prepreg plies: waviness due to air rich zones, plies that were not correctly orientated, misleading the direction of the vacuum compaction. The second aspect results in a difference of fibre tension within each 3 plies sequence, as the first ply is applied on a vacuum compacted surface, and the two subsequent plies on an heterogeneously manually compacted surface. Similar observations concerning the compaction method and the resulting ILTS were made by Charrier [23] for L-beam specimens with different ply orientations. The authors studied two different specimen types whose major difference was based on the intermediate debulking. They applied intermediate debulking every fourth to sixth ply on the first L-beam type and every second ply on the second L-beam type. They stated that the ILTS of the second L-beam type was 10 % higher than that of the first one.

The compaction irregularity during layup has three consequences. The first one are

small geometrical irregularities that resulted from the manual layup. As intermediate debulking is realised at 0.9 bar, and autoclave curing at 7 bar, the impact of the surface irregularities after layup were exacerbated by curing. In comparison, the panel surface after layup by the robot was sufficiently uniform to ensure a compaction normally to the mould during autoclave curing. The caul-plate stiffness was sufficiently high to correct the irregularities on the AFP panel, but not those of the MAN L-beam one. The second consequence is the result of these geometrical irregularities that happened during curing, and can be interpreted as an uncontrolled resin flow generated by an heterogeneous compaction. Some of the resin in the curved segment of the L-beam panel migrated to the arms of the L-beam, resulting in a fibre volume fraction variation through the span of the panel. The resin content has decreased in the curved part of the L-beam panel where a resin/interface based property is measured. The last consequence comes from the initial reason why intermediate debulking is applied during the prepreg layup: avoiding blocked air that can lead to porosity after autoclave curing. The porosity levels are similar (much less than 1% globally) for both MAN and AFP samples. Yet, larger areas of localised porosities between the plies are found in MAN samples compared to AFP samples. A last difference lies in the fact that, during tape deposition for AFP, the previous layer of tapes is reheated by the robot head to $\sim 25°C$. This lowers the viscosity and increases tacking. This strategy is very efficient for increasing adhesion between layers.

It can thus be concluded, that the AFP manufacturing process has a high influence on various parameters such as the specimen geometry and possible induced defects such as porosities, due to key features of AFP: compaction at every ply, and enhanced tacking between layers.

4.2. Influence of manufacturing process on failure location and ILTS

For AFP specimens, ILTS values are rather homogeneous and the failure locations are those expected by analytical or numerical estimations. There is no weak area such as large zones of localised porosity, which is rather diffuse and located between the tapes. The crack path is translaminar, running through different plies and exhibiting many branches. In contrast, the MAN manufacturing process of L-beam specimens with

such short radiuses is very intolerant to the smallest layup defects that will vastly affect the dimensional stability of even simple parts. ILTS values are $\sim$ 40 % lower than the AFP ones and more scattered (17 vs 6 %). This scattering is related to samples for which the ILTS value is low, the failure location different from the estimated one and for which relatively large zones of localised porosity are observed, and from which, most of the time, the crack originates. When ILTS is high, no such zones are observed, so that no "defect" (weak area) is at stake. For all MAN samples, the crack path is straight through the thickness and intralaminar. Still, the maximum value for MAN samples is lower than the minimum value of AFP samples. The enhanced bonding between plies during AFP processing is likely to be responsible for this.

Petersen et al. [24] carried out ILTS measurements following the standard used in this paper on thin ($\sim$ 3 mm) or thick ($\sim$ 8 mm) UD (M21/T700GC). They observed an increase in scatter with higher thickness in addition to a reduction of ILTS: 97 and 80 MPa for thin and thick samples, respectively. They also related a failure locus γ of 0.42 and 0.36 for thin and thick UDs respectively. In comparison to Lekhnitskii's estimation (our calculations), γ is found to be 0.42 and 0.34 for thin and thick UDs respectively. The authors related the scatter with a possible scale effect linked to a larger amount of voids. Charrier et al. [17] carried out the same measurements on the same material for thicknesses between $\sim$ 4 and 12 mm and observed no drastic reduction in ILTS: 47 and 40 MPa for thin and thick samples, respectively. However no information on the precise failure location was given apart from between one fourth and one half of the thickness. Makeev et al. [4] carried out ILTS measurements following the standard used in this paper on 6.3 mm in thickness UD (8552/IM7). They observed a large scatter in ILTS and in the failure locations ($\gamma \in [0.24; 0.59]$; the theoretical value being 0.37). They linked this variability to the presence of porosity. Indeed, by systematic use of computed tomography (CT) they associated the initiation of the crack to the presence of porosity. They also stated that this standard is not adequate for measuring ILTS and recommended the use of the short beam test. Manufacturing quality thick laminates by hand lay-up is a challenge. The use of ILTS from bending tests on curved beams seems to us more appropriate in a design sequence on curved composite parts such as hydrofoils since it is more representative (partially) of the process quality then

by using flat parts, for which the "true" ILTS can be measured.

None of our MAN L-beam specimens did break mechanically, i.e. at the radial position where the out-of-plane tensile stress is the highest, but due to defects and heterogeneities in the material, since porosities are observed. This in complete accordance with the latter studies [4, 17, 24]. The correspondance between experimental and theoretical failure locations in Petersen et al. [24] as well as the much higher ILTS values with respect to those from Charrier et al. [17] on the same material, in connection with Makeev et al. [4] observations of porosities, suggests that when there are some differences between estimated and measured failure locations, some defects (in this case porosities) are at stake and responsible for ILTS reduction.

In contrast, five out of seven AFP L-beam specimens broke at a location very close to estimations. For these AFP L-beam specimens it can thus be assumed that defects within the material were sufficiently small to exclude premature specimen failure during loading. The mechanical limit of those specimens could therefore be reached. It can hence be concluded that AFP L-beam specimens are more resistant than MAN ones of this study.

In order to estimate more accurately ILTS, the locations of the first failure cracks (on the edges), $r_{failure}$, were entered into the FE model, and $ILTS^{FE}$ ($r_{failure}$) were calculated. The results are given in Table 4 and summarised in Table 3. The resulting mean values (67.0±6.6 MPa for AFP and 35.6±5.4 MPa for MAN L-beam specimens) show that the difference in ILTS between AFP and MAN specimens increases to 46.8 %.

5. Conclusion

Unidirectional thick (13 mm) L-beam specimens were fabricated by hand lay-up (MAN) using classical nautical manufacturing conditions and by AFP technology from the same CFRP prepreg material and tested in four-points bending. MAN and AFP specimens were compared in terms of test reproducibility, specimen metrology and material bending stiffness, first failure crack locations, failure loads and Interlaminar Tensile Strengths (ILTS).

Specimens should theoretically fail at a given estimated specific location from the inner radius. All AFP specimens failed close to the estimated location. Their mechanical

limit had therefore been reached. By contrast, none of MAN specimens broke at the estimated location. Defects induced by the manufacturing process are localised porosities.

The 47 % lower ILTS values for MAN specimens, their scatter three times higher, as well as these failure locations different from the estimations, indicate that the MAN manufacturing process is more difficult to carry out for thick curved composite parts other than simple plates without inducing defects. Key features of AFP (staggering, compaction every ply, enhanced tacking by local heating) make it possible for composite structures to reach high ILTS values in a reproducible way.

Hydrofoils used in racing yachts are thick (up to 120 mm) and have a double curvature, which is less favourable for MAN manufacturing as compared to AFP, and is likely to promote the creation of defects such as porosities. In terms of applications of this study to hydrofoils, let us note that the internal radius of the samples are smaller that those the hydrofoils elbows. The smaller the radius the higher the swelling so that this work maximises this possibility.

Acknowledgments

We would like to thank A. Launay and A. Le Palabe (IRDL) for stimulating discussion and to K. Henry (IRMA) and R. Le Borgne (Avel Robotics) for experimental assistance. Région Bretagne and CD56 (project DURAFOIL) are acknowledged for the PhD. grant of M. Grabow.

References

[1] X. Xu, M. I. Jones, H. Ali, M. R. Wisnom, S. R. Hallett, Effect of out-of-plane wrinkles in curved multi-directional carbon/epoxy laminates, Compos. Sci. Technol. 197 (June) (2020) 108282.

[2] S. Qian, X. Liu, Y. Ye, Q. Xu, T. Zhang, X. Li, Effect of gap and overlap fiber placement defects on the delamination behavior of L-shaped composite laminates, Compos. Struct. 268 (April) (2021) 113963.

[3] W. Zhou, Q. Cheng, Q. Xu, W. Zhu, Y. Ke, Deformation and fracture mechanisms of automated fiber placement pre-preg laminates under out-of-plane tensile loading, Compos. Struct. 255 (September 2020) (2021) 112948.

[4] A. Makeev, G. Seon, Y. Nikishkov, E. Lee, Methods for assessment of interlaminar tensile strength of composite materials, J. Compos. Mater. 49 (7) (2015) 783–794.

[5] Y. Nikishkov, G. Seon, A. Makeev, Structural analysis of composites with porosity defects based on X-ray computed tomography, J. Compos. Mater. 48 (17) (2014) 2131–2144.

[6] W. C. Jackson, P. G. Ifju, Through-the-Thickness Tensile Strength of Textile Composites, in: R. B. Deo, C. R. Saff (Eds.), Composite Materials: Testing and Design: Twelfth Volume, ASTM International, West Conshohocken, PA, ISBN 978-0-8031-5331-8, 218–238, 1996.

[7] ASTM D6415 / D6415M-06a, Standard Test Method for Measuring the Curved Beam Strength of a Fiber-Reinforced Polymer-Matrix Composite, URL www.astm.org, 2013.

[8] S. G. Lekhnitskii, Anisotropic plates, Gordon & Breach; Reprint edition (January 1, 1968), ISBN 978-0677206707, 1968.

[9] K. Kedward, R. Wilson, S. McLean, Flexure of simply curved composite shapes, Composites 20 (6) (1989) 527–536, ISSN 0010-4361.

[10] H. McManus, Y.-P. Mak, Strain rate and manufacturing technique effects on the damage tolerance of composite laminates, in: 34th Structures, Structural Dynamics and Materials Conference, 1993.

[11] M. Lan, D. Cartié, P. Davies, C. Baley, Microstructure and tensile properties of carbon–epoxy laminates produced by automated fibre placement: Influence of a caul plate on the effects of gap and overlap embedded defects, Composites Part A: Applied Science and Manufacturing 78 (2015) 124–134, ISSN 1359-835X.

[12] M. H. Nguyen, A. A. Vijayachandran, P. Davidson, D. Call, D. Lee, A. M. Waas, Effect of Automated Fiber Placement (AFP) Manufacturing Signature on Mechanical Performance, in: AIAA Scitech 2019 Forum, 2019.

[13] A. Marchandise, Impact of manufacturing processes on the critical mechanical performances of a hydrofoil. Implementation of automated solutions [in French], Ph.D. thesis, Univ. Bretagne Sud, France, 2020.

[14] K. Kozaczuk, Automated fiber placement systems overview, Prace Instytutu Lotnictwa Nr 4 (245) (2016) 52—-59.

[15] M. Lan, Étude de l'influence des singularités créées par la technique de placement de fibres automatisé sur les performances des matériaux composites [in French], 2016.

[16] K. D. Potter, Understanding the origins of defects and variability in composites manufacture, in: International conference on composite materials (ICCM)-17, Edinburgh, UK, 18–25, 2009.

[17] J.-S. Charrier, F. Laurin, N. Carrere, S. Mahdi, Determination of the out-of-plane tensile strength using four-point bending tests on laminated L-angle specimens with different stacking sequences and total thicknesses, Composites Part A: Applied Science and Manufacturing 81 (2016) 243–253.

[18] W. C. Jackson, R. H. Martin, An Interlaminar Tensile Strength Specimen, in: E. T. Camponeschi (Ed.), Eleventh Volume: Composite Materials—Testing and Design, ASTM International, West Conshohocken, PA, ISBN 978-0-8031-5252-6, 333–354, 1993.

[19] D. Ranz, J. Cuartero, A. Miravete, R. Miralbes, Experimental research into interlaminar tensile strength of carbon/epoxy laminated curved beams, Composite Structures 164 (2017) 189–197.

[20] D. Gay, S. V. Hoa, S. W. Tsai, Composite materials : design and applications, CRC Press, Boca

Raton, FL, second edition. edn., ISBN 9781420045192, 2007.

[21] C. T. Rueden, J. Schindelin, M. C. Hiner, B. E. DeZonia, A. E. Walter, E. T. Arena, K. W. Eliceiri, ImageJ2: ImageJ for the next generation of scientific image data, BMC bioinformatics 18 (1) (2017) 1–26, ISSN 1471-2105.

[22] V. Keryvin, A. Marchandise, P.-Y. Mechin, J.-C. Grandidier, Determination of the longitudinal non linear elastic behaviour and compressive strength of a CFRP ply by bending tests on laminates, Composites Part B: Engineering 187 (2020) 107863.

[23] J.-S. Charrier, Développement de méthodologies dédiées à l'analyse robuste de la tenue de structures composites sous chargements complexes tridimensionnels [in French], Ph.D. thesis, ENSAM, France, 2013.

[24] E. Petersen, E. Kappel, J. Koord, O. Völkerink, C. Hühne, Determination of stresses, strains and failure types in multidirectional laminates under pure bending, J. Compos. Mater. 54 (28) (2020) 4397–4413.

Table 1 Metrology mean values of AFP and MAN specimens. w, t, r_i, r_o, L, Φ_i are respectively, the width, thickness, internal and outer radii, arm length and initial half-angle of L-beam.

Mean values	w_{mean}	t_{mean}	$t_{max,mean} - t_{min,mean}$	$r_{i,mean}$	$r_{o,mean}$	L_{mean}	$\Phi_{i,mean}$
	[mm]	[mm]	[mm]	[mm]	[mm]	[mm]	[°]
AFP	24.68	12.89	0.87	5.99	18.9	110	45
MAN	25.10	13.16	1.60	6.02	19.2	110	45
Difference [%]	1.7	2.1		0.5	1.7	0	0

Table 2 Elastic properties of SE84LV/IM2C ply (transverse isotropy)

E_1	E_2	ν_{12}	ν_{23}	G_{12}	G_{23}
[MPa]	[MPa]	[-]	[-]	[MPa]	[MPa]
160000	8000	0.3	0.3	4000	3077

Table 3 Summary of results between AFP and MAN L-beam specimens tested in 4PB.

	AFP	Difference	MAN
Mean stiffness [N/mm]	3743 ± 104	0.3 %	3735 ± 104
Mean load at failure [N]	6661 ± 427	40.2 %	3983 ± 740
Location of first failure crack	5/7 at r_{max}	-	0/7 at r_{max}
Number of edge cracks	1-6 (mean 3)	-	1
$ILTS^{FE}$ (r_{max}) [MPa]	76.7±5.5	43.0 %	43.7±8.0
$ILTS^{FE}$ ($r_{failure}$) [MPa]	67.0±6.6	46.8 %	35.6±5.4

Table 4 First failure cracks locations ($r_{failure}$, edges). Confrontation of analytical (superscripts K Eq. (8) and L Eq. (5)) and numerical (FE, for r_{max}, Eq. (7) and ($r_{failure}$)) ILTS of AFP and MAN L-beam specimens. Numbers in bold indicate that $r_{failure}$ is close to r_{max}.

Sample		First failure crack $\gamma = \frac{r_{failure} - r_i}{t}$ [-]	$ILTS^K$ [MPa]	$ILTS^L$ [MPa]	$ILTS^{FE}$ (r_{max}) [MPa]	$ILTS^{FE}$ ($r_{failure}$) [MPa]
AFP lay-up	1	0.57	79.1	68.9	81.7	58.4
	2	**0.33**	73.4	65.5	77.1	70.0
	3	**0.36**	73.4	65.8	77.0	69.4
	4	0.17	66.8	59.4	67.6	57.2
	5	**0.33**	68.2	61.0	67.7	65.2
	6	**0.33**	79.9	71.1	82.8	75.2
	7	**0.36**	75.4	67.1	80.9	73.8
Mean value			73.7±4.6	65.5±3.8	76.7±5.5	67.0±6.6
MAN lay-up	1	0.38	57.1	50.8	58.3	42.3
	2	0.38	49.0	43.3	47.2	42.0
	3	0.50	47.3	41.9	47.2	37.6
	4	0.55	41.3	36.9	41.0	30.9
	5	0.43	32.0	28.4	31.3	26.7
	6	0.43	44.5	39.4	43.6	37.4
	7	0.19	37.3	32.9	36.9	32.5
Mean value			44.1±7.6	39.1±6.8	43.7±8.0	35.6±5.4
Difference AFP - MAN			40.2 %	40.3 %	43.0 %	46.8 %

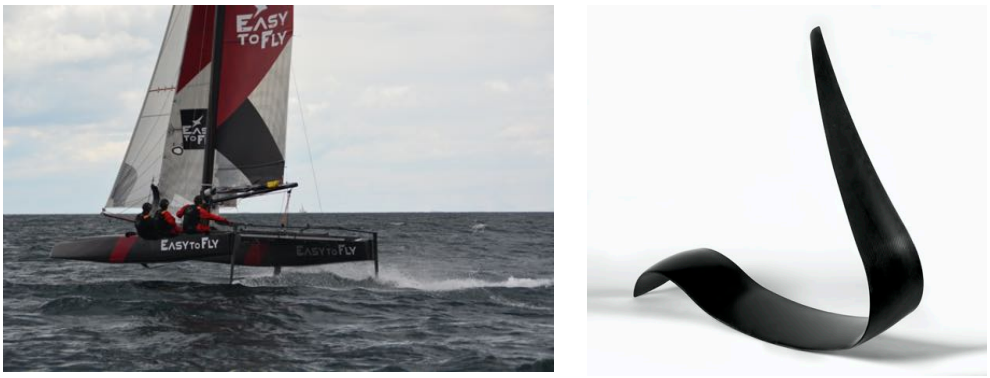

Fig. 1. Hydrofoils manufactured by AFP in January 2017: (left) during sailing with ETF26 class catamaran and (right) after manufacturing (Avel Robotics).

Fig. 2. AFP L-beam specimen production. the arrow indicates the direction of the fibres.

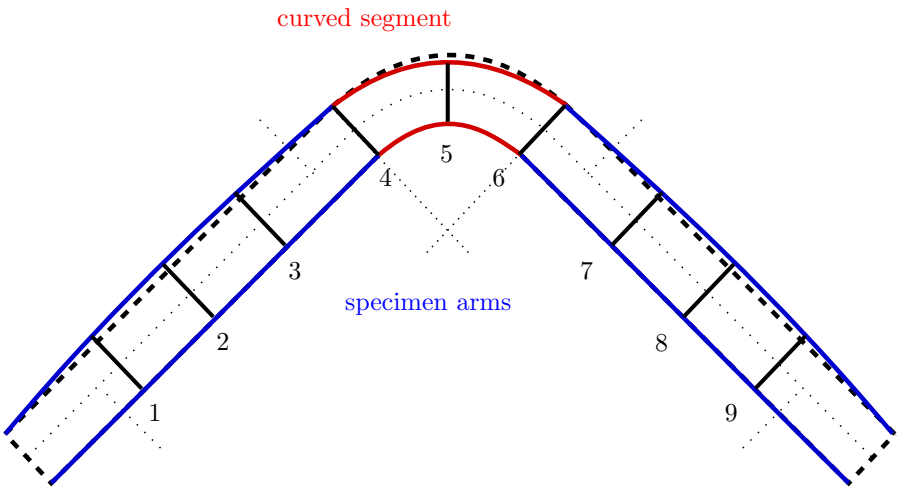

Fig. 3. Locations of the different thickness measurements after curing. The blue lines indicate a higher thickness in the arms while the red lines indicate a lower thickness in the curved part of the L-beam, which is observed for MAN specimens.

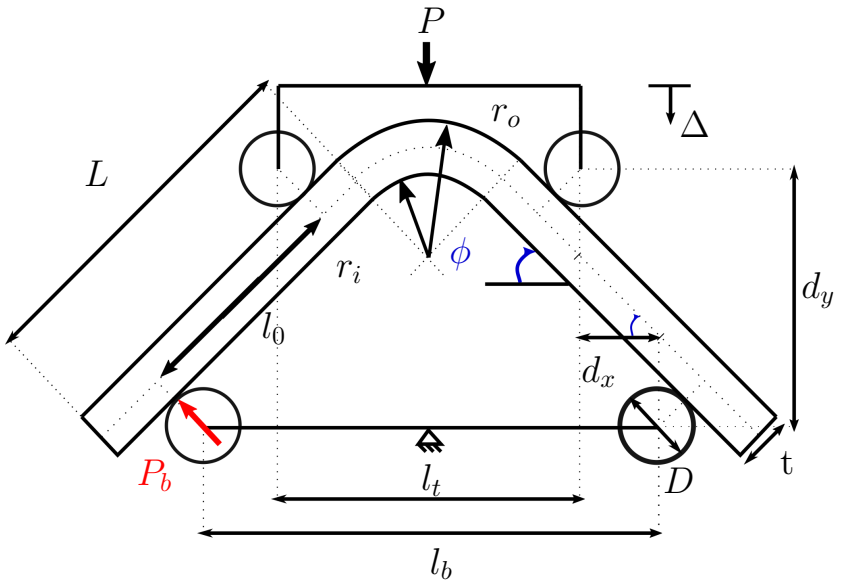

Fig. 4. 4PB test setup for ILTS determination.

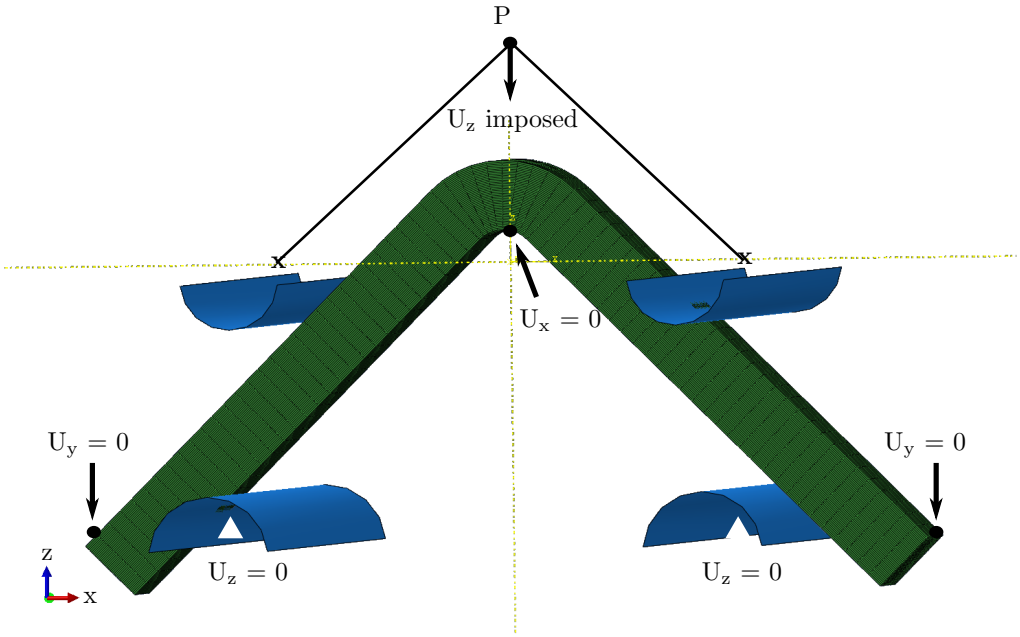

Fig. 5. Numerical model of the 4PB on L-beam with boundary conditions.

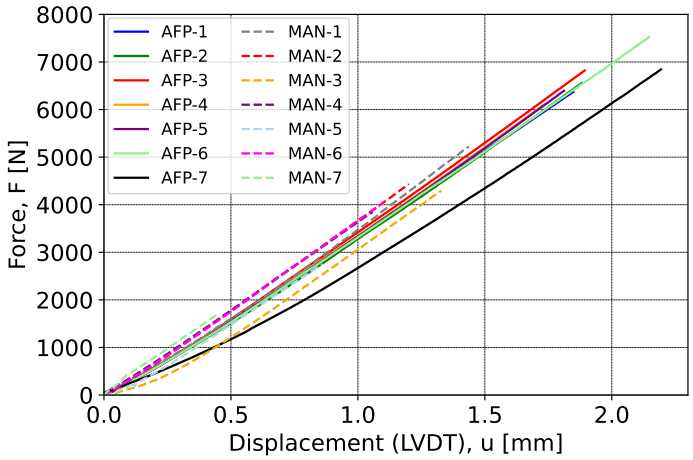

Fig. 6. Experimental load-displacement plots of AFP and MAN L-beam specimens. Only data before load drop were kept.

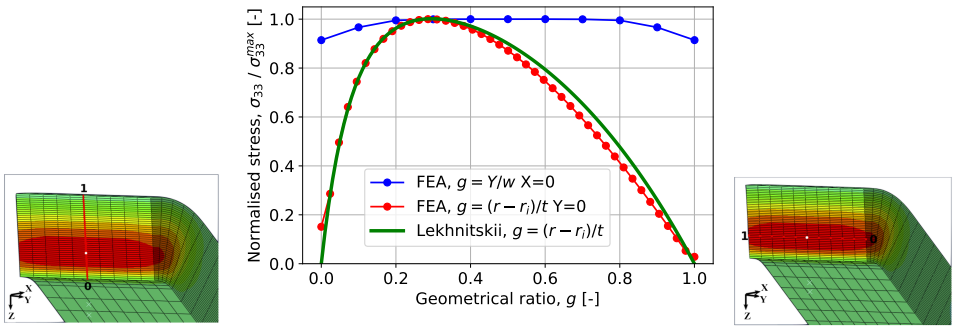

Fig. 7. Normalised out-of-plane tensile stress. FEA results vs normalised thickness and height. Analytical plane strain solution of Lekhnitskii vs normalised thickness.

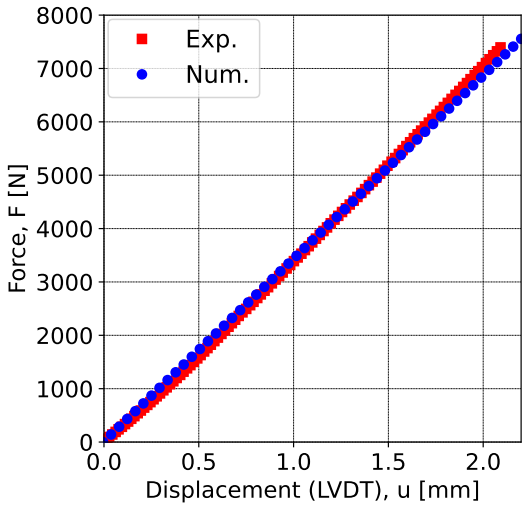

Fig. 8. Confrontation of experimental/numerical force-displacement diagram of L-beam specimen AFP-06.

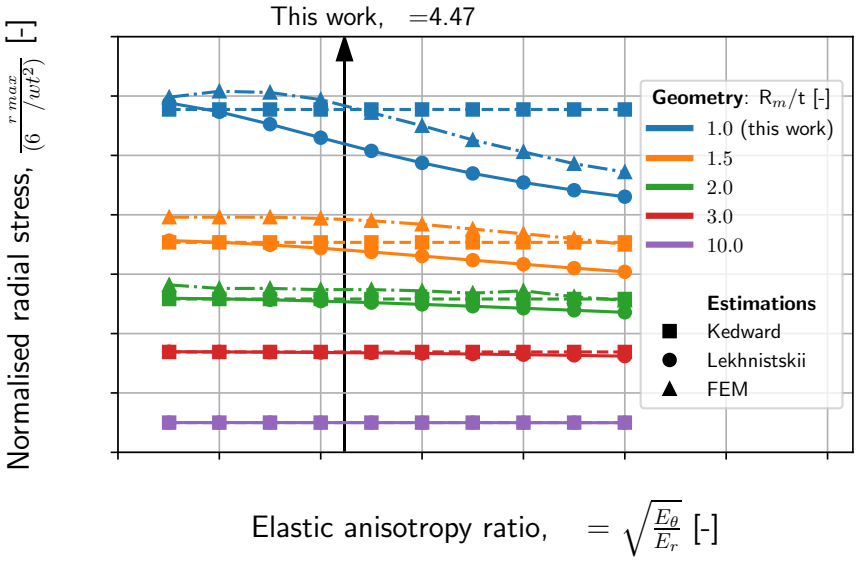

Fig. 9. Maximum normalised radial stress as a function of the degree of anisotropy κ and the specimen geometry. Colors are for the ratio R_m (mean radius) to thickness t. Dotted lines represent Kedward et al. [9] solution, solid lines with dots Lekhnitskii [8] solution, and the triangles represent the FE simulation. Kedward et al. [9] solution is close to the numerical calculation due to the specific elastic properties of the material.

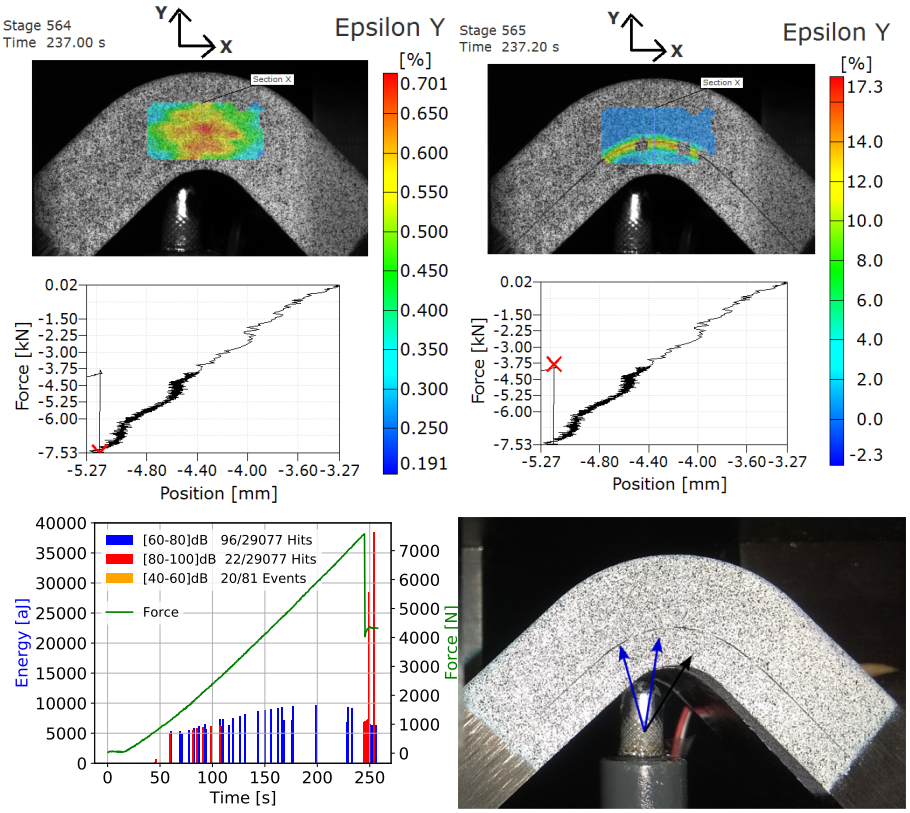

Fig. 10. Example of the experimental results on a sample (AFP-6) introducing the different instrumentation sensors. (Up) Correlation between DIC and mechanical response. (Bottom) Correlation between AE and mechanical response. Post-mortem observation with the arrows indicating the position of the cracks.

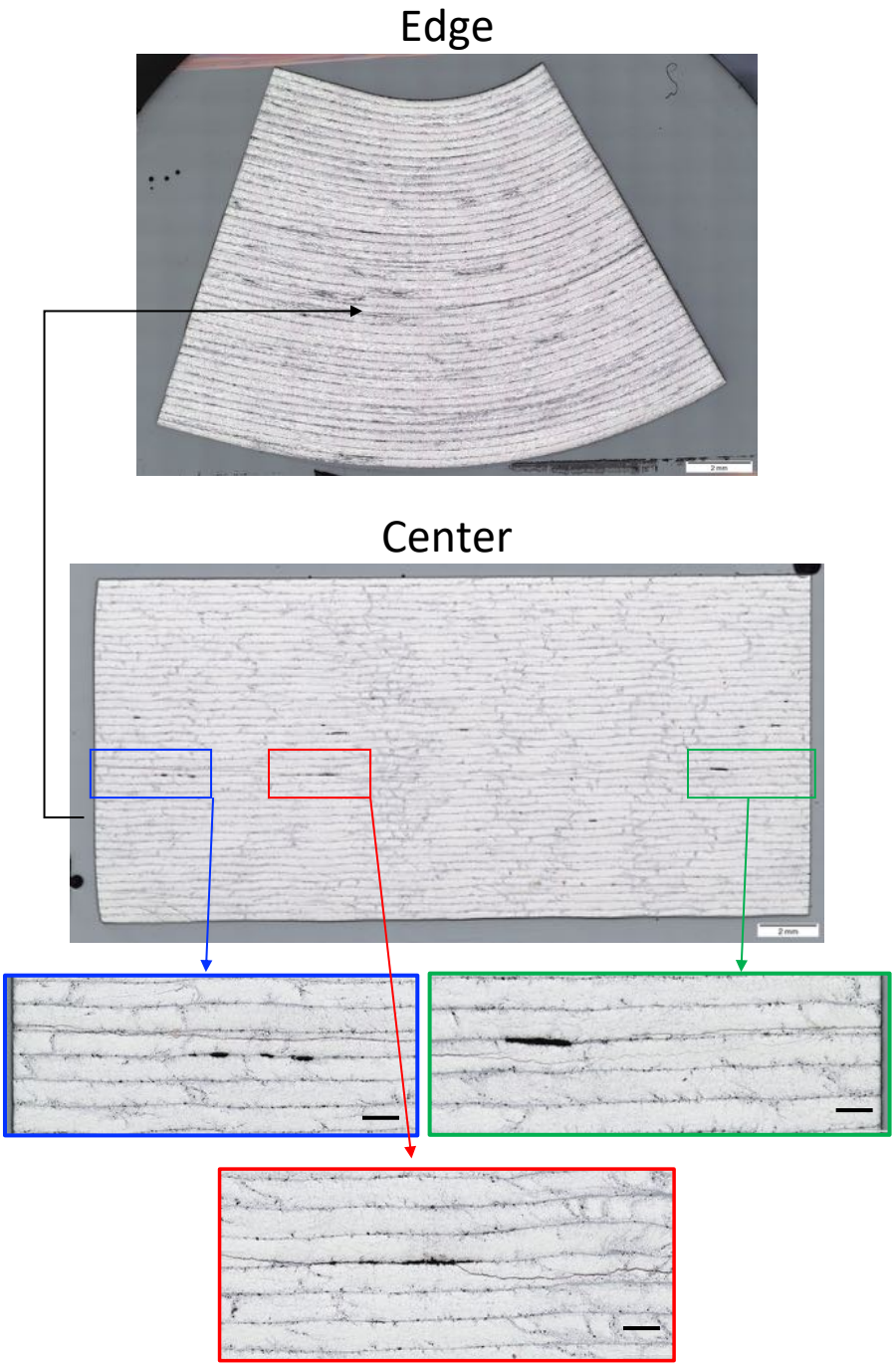

Fig. 11. Optical micrographs of the polished edge (top) and cross-section of sample MAN-4 (bottom) with associated magnifications on the main crack at the free surface (bottom). (The mould side is at the top. The black ruler stands for 200 μm.)

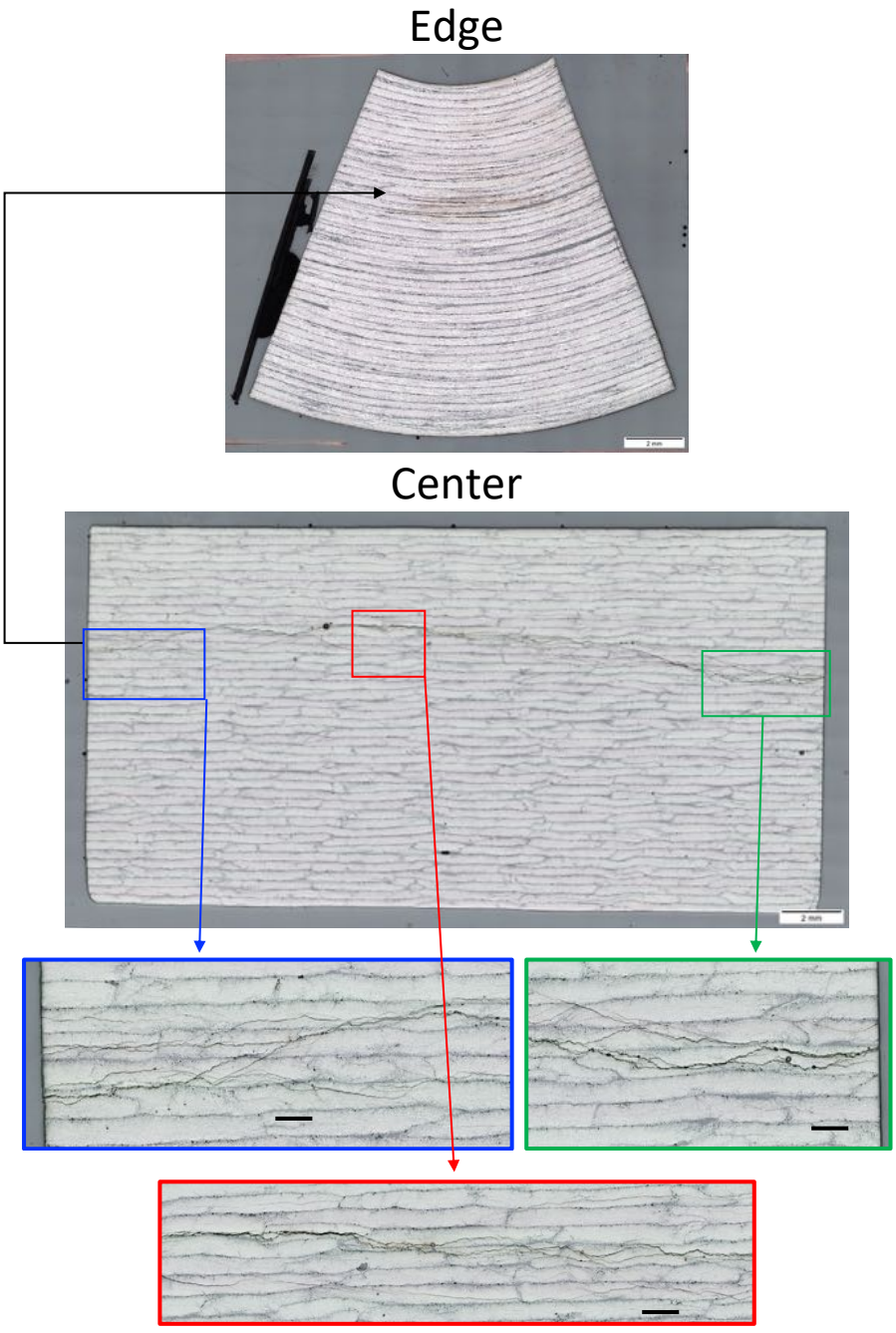

Fig. 12. Optical micrographs of the polished edge (top) and cross-section of sample AFP-6 (bottom) with associated magnifications on the main crack at the free surface (bottom). Except for the porosity at the bottom, the other black circles are polishing artefacts and not porosities. (The mould side is at the top. The black ruler stands for 200 μm.)

Methodology, Validation, Writing - Original Draft, Writing- Reviewing and Editing, Supervision, Validation.
Adrien Marchandise: Resources, Conceptualization, Writing-Reviewing and Editing.
Jean-Claude Grandidier*:* Writing-Reviewing and Editing, Validation.
Christophe Baley: Writing-Reviewing and Editing
Cyran Le Guennec: Methodology, Investigation.
Odran Fagherazzi: Software.

Declaration of interests

☒ The authors declare that they have no known competing financial interests or personal relationships that could have appeared to influence the work reported in this paper.

☐The authors declare the following financial interests/personal relationships which may be considered as potential competing interests: